Supplementary Materials

Atmospheric heterogeneous reaction of chlorobenzene on mineral α-fe_2o_3 particulates: a chamber experiment study

Meiling Chen[1,2], Mengjie Yin[3], Yuetan Su[1], Ruizhe Li[1], Kezhou Liu[3], Zhongbiao Wu[1,4], Xiaole Weng (✉)[1,2,4]

1 Key Laboratory of Environment Remediation and Ecological Health (Ministry of Education), College of Environmental and Resource Sciences, Zhejiang University, Hangzhou 310058, China
2 ZJU-Hangzhou Global Scientific and Technological Innovation Center, Zhejiang University, Hangzhou 311215, China
3 School of Automation (School of Artificial Intelligence), Hangzhou Dianzi University, Hangzhou 310018, China
4 Zhejiang Provincial Engineering Research Centre of Industrial Boiler & Furnace Flue Gas Pollution Control, Hangzhou 311200, China

.

Summary of the Appendix: 31 Pages, 6 Tables and 11 Figures

✉Corresponding author
E-mail: xlweng@zju.edu.cn

Methods

S1. Chamber Experiments

Chamber experiments were mainly conducted to explore the degradation rates and the byproducts of chlorobenzene (CB) on the α-Fe_2O_3 surface under different conditions, including interference from SO_2 or NO_2. The chamber reactions were performed in an airtight reaction chamber, where the quantitative α-Fe_2O_3 powder (0.15 g) was coated onto a sample stage with the assistance of absolute ethanol and a certain amount of gaseous reactants were introduced by a mobile injector. The gases were stirred in the dark until they were evenly mixed, and then turned on the lamp for illumination. The reaction temperature was always held at 30 °C through the circulating water. And the reaction humidity (RH) was the actual atmospheric humidity (at approximately 60%-80%). While the regulation of RH was achieved by air (pure, Hangzhou Jingong Special Gas Co., Ltd., Hangzhou, China) bubbling for 1 h at the speed of 100 mL/min. A GC9790 II gas chromatograph (Zhejiang Fuli Analytical Instrument Co., Ltd., Taizhou, China) was used to monitor the CB concentration. Assuming that CB was homogenously mixed in the chamber and always present in excess, the changes in CB concentration can be fitted by a pseudo-first-order kinetics equation:

$$\ln[C/C_0]=-kt \quad (1)$$

where t (h) is the time of CB exposure in the chamber, $[C/C_0]$ is the CB concentration normalized to the initial CB concentration, and k is the decay rate of CB in the chamber.

Besides, the byproducts were enriched in the reaction chamber, where the reactants were reacted with α-Fe_2O_3 for 7 h under irradiation. Particularly, the samples for chlorophenol and polychlorinated dibenzo-*p*-dioxin and dibenzofuran (PCDD/F) measurements were treated for 35 h (involving 5 cycles with each cycle lasting for 7 h) under consistent conditions to obtain the PCDD/Fs with a detectable level.

S2. Density Functional Theory Calculations

The density functional theory (DFT) calculations in this study were performed by using the Vienna ab initio simulation package (VASP) (Kresse and Hafner, 1993,1994; Kresse and Furthmuller, 1996) with a Perdew-Burke-Ernzerhof functional (Perdew et al., 1996). Spin-polarized DFT was performed to describe the magnetic properties of α-Fe_2O_3, and the antiferromagnetic

arrangement was set. DFT+U was used in this study to describe the *3d* states of α-Fe_2O_3 properly, which tends to be inaccurately represented in standard DFT. The Hubbard U correction for ferrum was set to 4 eV (U = 5 eV and J = 1 eV), as tested by previous studies (Feng et al., 2020a,b). The cutoff energy with the projector augmented wave (PAW) (Blochl, 1994) method of the system was set to 500 eV. A (3 × 3) supercell of the α-Fe_2O_3 (001) surface (15.31 Å × 15.31 Å) with 54 Fe atoms and 81 O atoms was used as the substrate. Only the Γ point of the Brillouin zone (1 × 1 × 1) was sampled for integration in reciprocal space to balance the accuracy and speed because the system had more than one hundred atoms. The vacuum space was set to at least 20 Å to minimize interlayer interaction. In geometrical optimization, the bottom six layers were fixed in their bulk position, while the other layers were permitted to relax. The SCF energy convergence was set to 1E-05 eV, and the forces on each atom were smaller than 0.02 eV $Å^{-1}$.

The configuration was optimized geometrically to obtain the most stable adsorption configuration with the lowest energy. To understand the adsorption of the gas molecule on the substrate catalyst, the adsorption energy (E_{ad}) was defined as:

$$E_{ad}=E_{adsorbate/substrate}-E_{adsorbate}-E_{substrate} \quad (2)$$

where a negative value corresponds to an exothermic process.

S3. Chlorophenol Test

The chlorophenols remaining on the surface were extracted using dichloromethane, where 10 mL of dichloromethane and 0.8 g reacted α-Fe_2O_3 (35 h) were mixed in a glass bottle and ultrasonically oscillated for 40 min in an ice bath. Then, the extracted liquid was transferred into a test tube and concentrated to 1 mL by a nitrogen blower. Finally, the liquid was filtered, and 0.5 μL was injected into a GC/MS system (7890A GC, 5975C MS, Agilent Technologies, California, United States) with a DB-624 (30 m × 0.32 mm *i.d.* × 1.8 μm film thickness, 6% cyanopropyl-phenyl/94% dimethylpolysiloxane, Agilent Technologies, California, United States) capillary column. The GC oven was initially held at 35 °C for 4 min, then increased to 60 °C (15 °C/min), and finally rose to a final temperature and held for 5 min (220 °C, 17 °C/min). MS was performed in the electron impact ionization mode using selected ion monitoring (SIM). The temperature of the ion source was set to 230 °C.

S4. Characterizations

The surface chemical compositions were analyzed using a X-ray photoelectron spectroscopy (XPS) (Escalab 250, Thermo Fisher Scientific, Massachusetts, United States) equipped with Al Kα radiation (150 W), and the binding energy scale for each sample was calibrated by the signal of adventitious carbon (binding energy at 284.8 eV). The electron paramagnetic resonance (EPR) spectra were recorded using a JES-FA200 EPR spectrometer (JEOL, Tokyo, Japan) at room temperature. X-ray powder diffraction (XRD) patterns were recorded using a D/Max RA diffractometer (Rigaku, Japan) with Cu-Kα radiation (λ = 0.15418 nm) at 40 kV and 150 mA. BET surface area measurements were determined using N_2 physisorption at 77 K with a Micrometrics ASSP 2020 equipment. Prior to N_2 adsorption, each sample was outgassed under vacuum at 200 °C for 2 h.

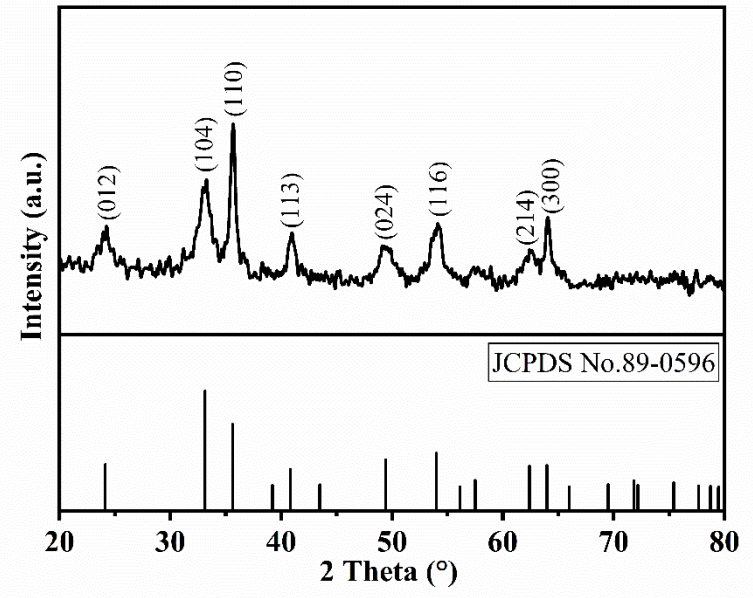

Figure S1. XRD patterns of the fresh α-Fe_2O_3.

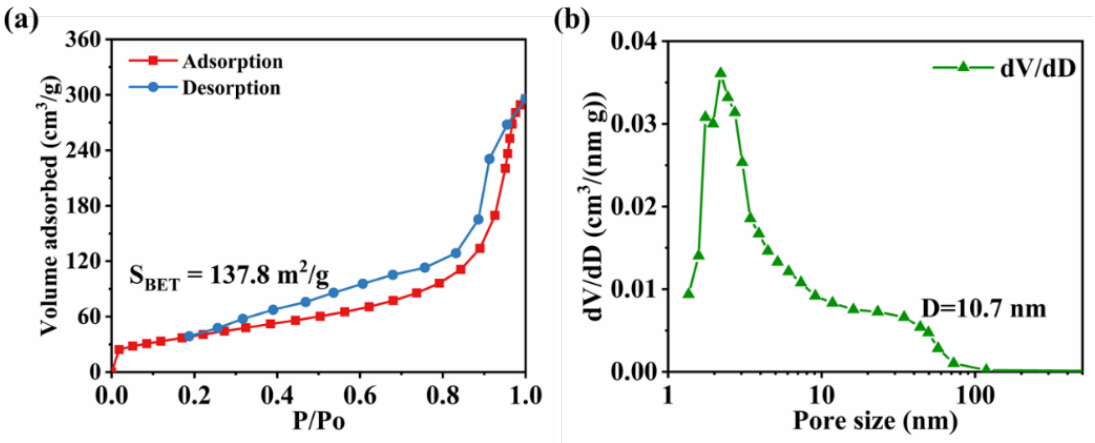

Figure S2. The test results of specific surface area of α-Fe2O3. (a) The adsorption isothermal curve. (b) Pore size distribution.

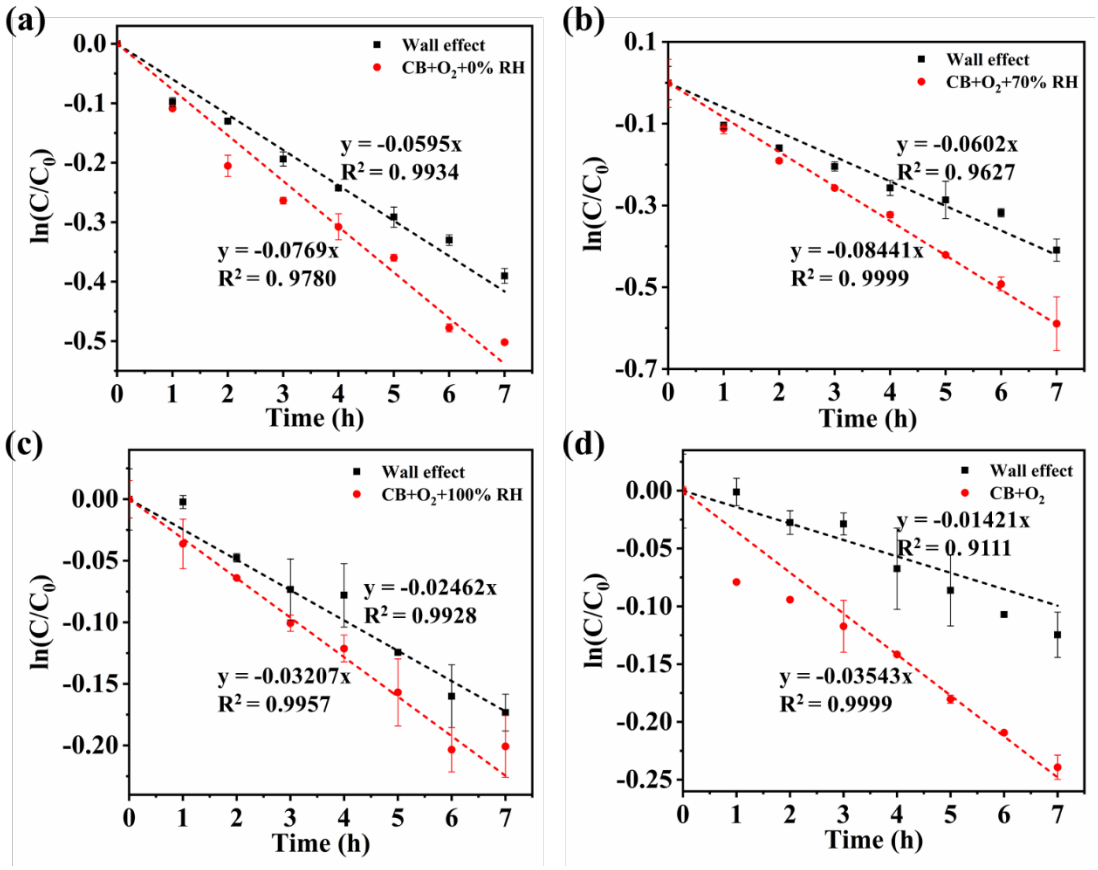

Figure S3. Decay rates of CB in the absence and presence of the α-Fe2O3 particulates under different relative humidity in chamber experiments. (a) 0% RH; (b) 70% RH; (c) 100% RH; (d) the CB + O2 reaction under the ambient RH. Reaction conditions: [CB] = 200 ppm, air balance, 30 °C and xenon light irradiation (λ = 320–780 nm). Error bars represent standard deviation.

To evaluate the effects of relative humidity (RH), we further conducted a series of additional chamber experiments under different humidity conditions, with the relative humidity (RH) at 0%, 70% and 100%. As shown in **Figure A3** and **Table A2**, the degradation rate of CB under 70% RH was relatively similar to that under actual atmospheric humidity. When the RH was 0%, the decay rate of CB was slightly decreased, originating the lack of hydroxyl radicals. However, when the RH increased to 100%, the decay rate of CB was significantly inhibited, presumably owing to the particle surface has been covered with a water film (Han et al., 2014). We also calculated the adsorption energy of H_2O on the α-Fe_2O_3 (001) surface by using DFT, and found that its adsorption energy was -6.441 eV, which was close to that of CB (E_{ad} = -6.557 eV), showing competitive adsorption as the SO_2 does.

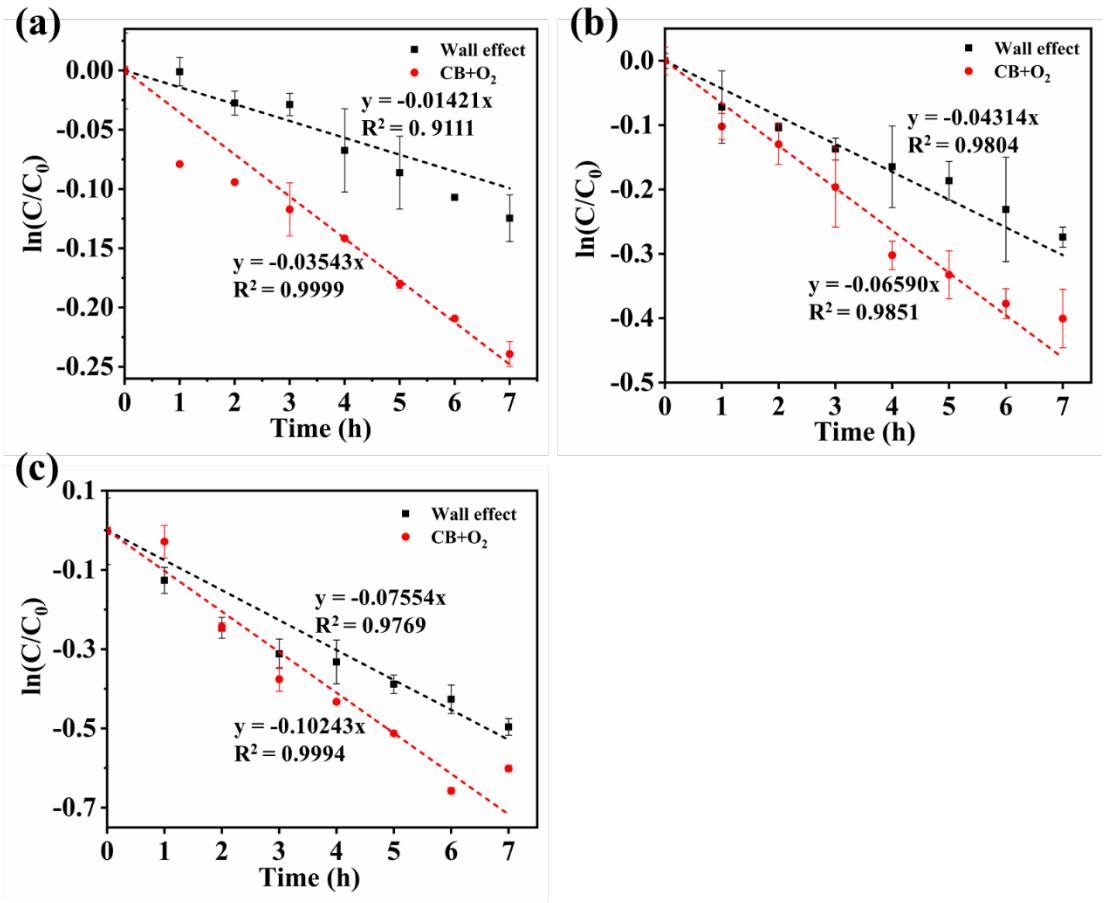

Figure S4. Decay rates of CB in the absence and presence of the α-Fe_2O_3 particulates under different initial CB concentrations in chamber experiments. (a) 200 ppm; (b) 100 ppm; (c) 50 ppm. Reaction conditions: air balance, 30 °C and xenon light irradiation (λ = 320–780 nm). Error bars represent standard deviation.

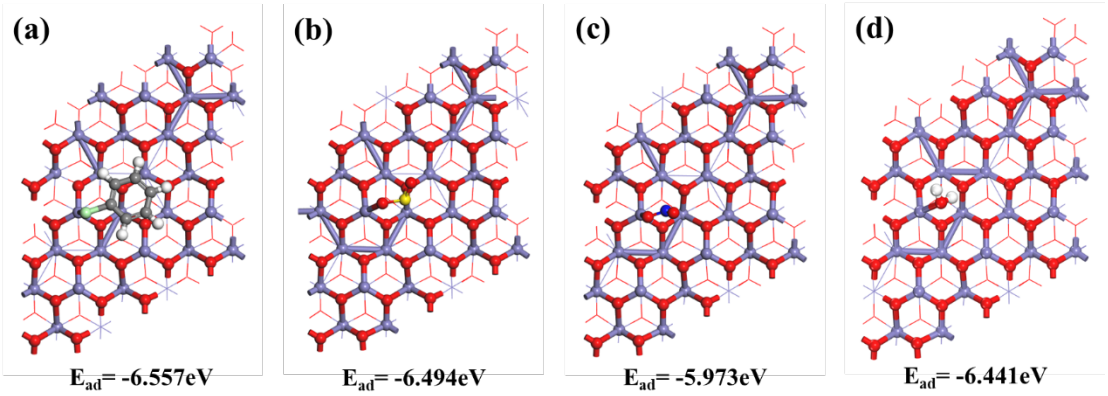

Figure S5. Optimized structures of different reaction gases on α-Fe_2O_3 (001). **(a)** CB; **(b)** SO_2; **(c)** NO_2; **(d)** H_2O. Iron atoms are purple balls, oxygen atoms are red balls, carbon atom are gray balls, hydrogen atoms are white balls, chlorine atom is green ball, sulfur atom is yellow ball, nitrogen atom is blue ball.

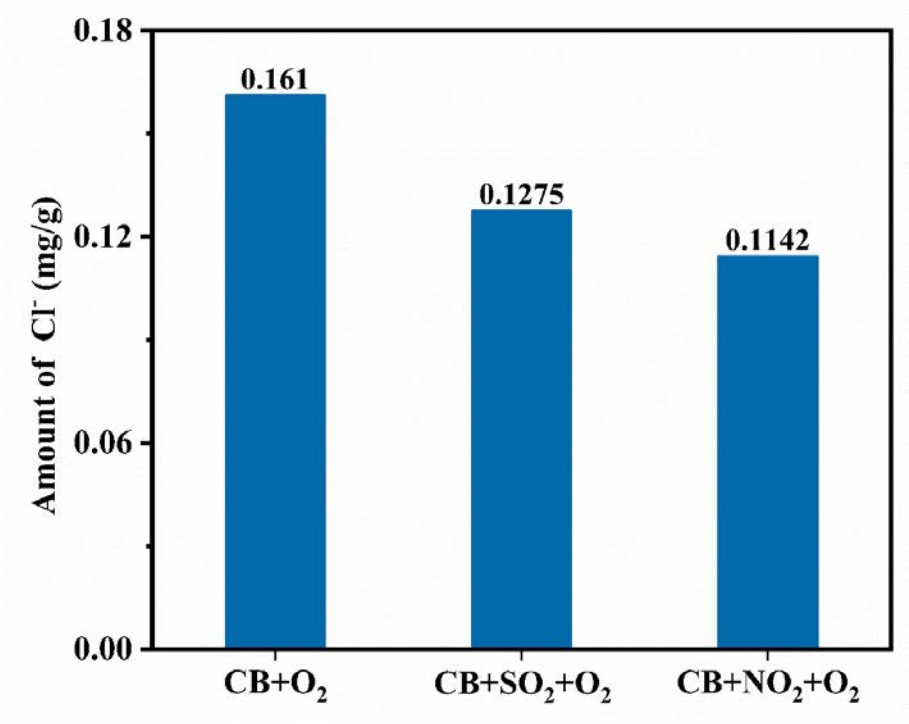

Figure S6. Cl- analyses on the reacted α-Fe_2O_3 under different reaction conditions. Reaction conditions: [CB] = 200 ppm, [SO_2] = [NO_2] = 50 ppm, air balance, 30 °C, 7 h and xenon light irradiation (λ = 320-780 nm).

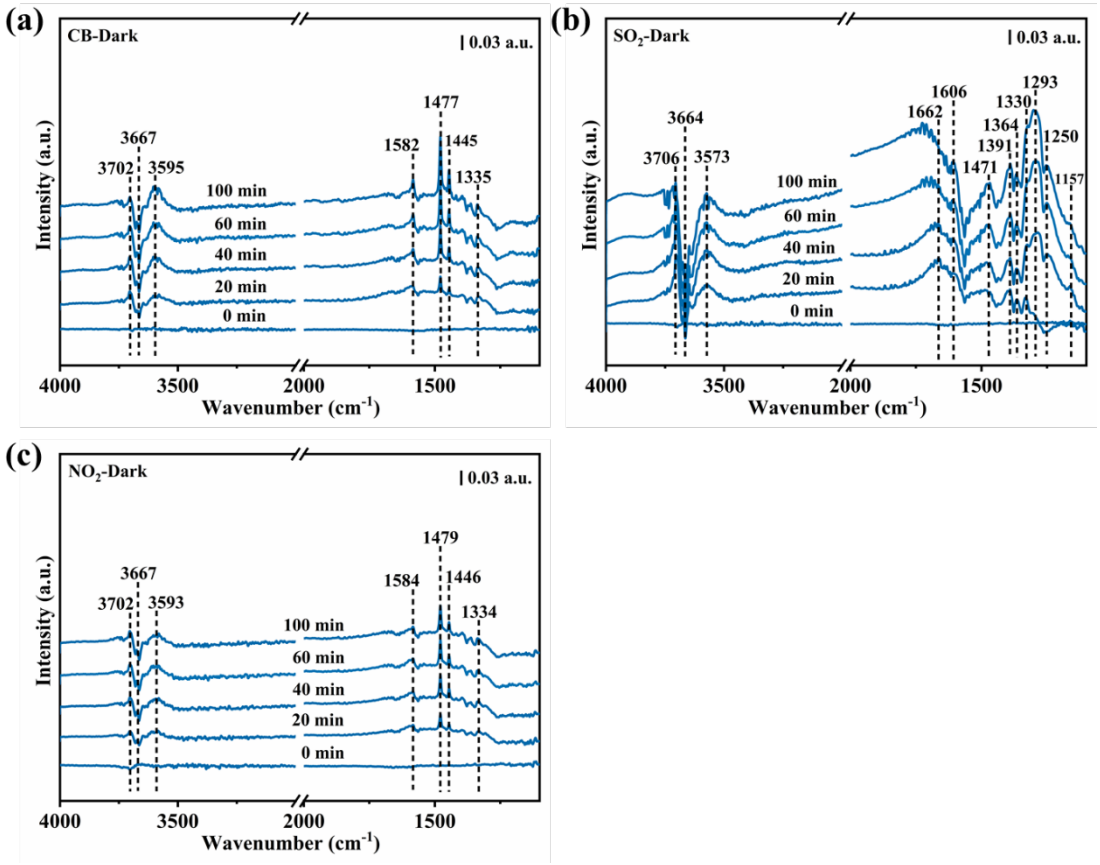

Figure S7. In situ DRIFT spectra of α-Fe_2O_3 as a function of time with a flow of CB or SO_2 or NO_2 under the dark state. Reaction conditions: [CB] = 200 ppm, [SO_2] = [NO_2] = 50 ppm, He balance, 30 °C.

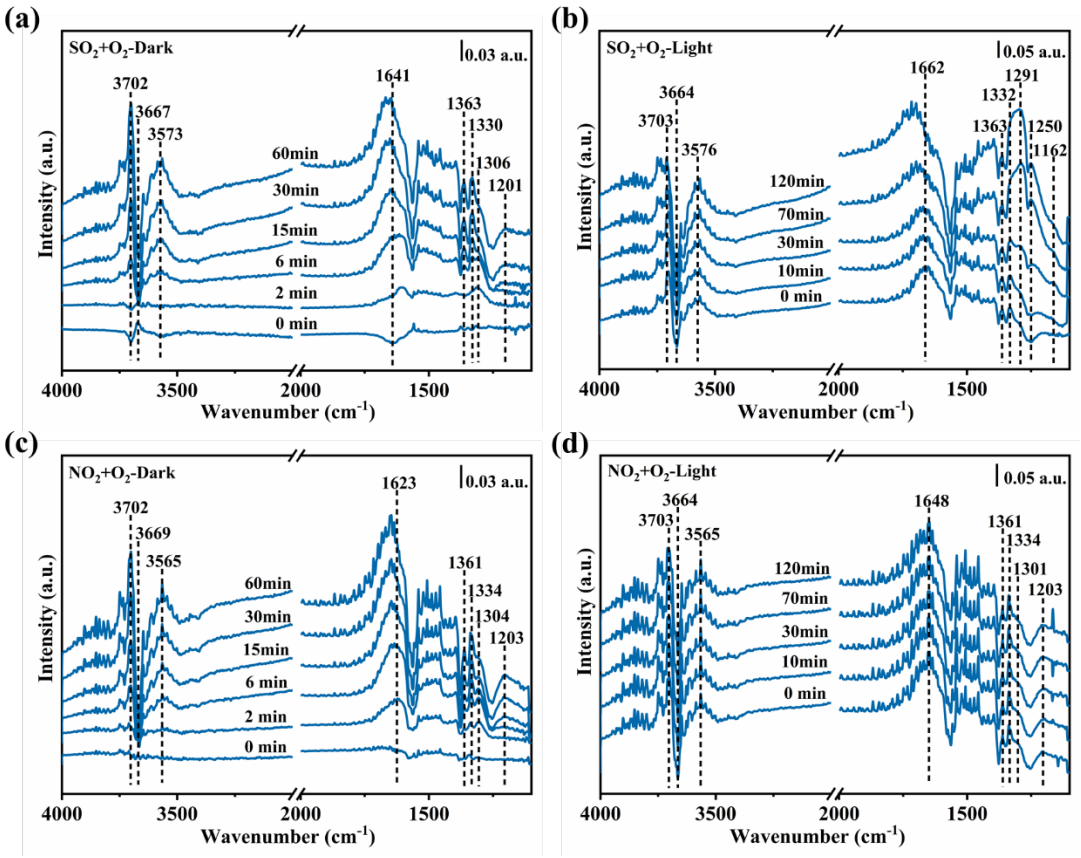

Figure S8. In situ DRIFT spectra of α-Fe_2O_3 as a function of time with a flow of 50 ppm SO_2 or NO_2 in the absence and presence of light. Reaction conditions: [SO_2] = [NO_2] = 50 ppm, [O2] = 20 vol %, He balance, 30 °C and xenon light irradiation (λ = 320–780 nm).

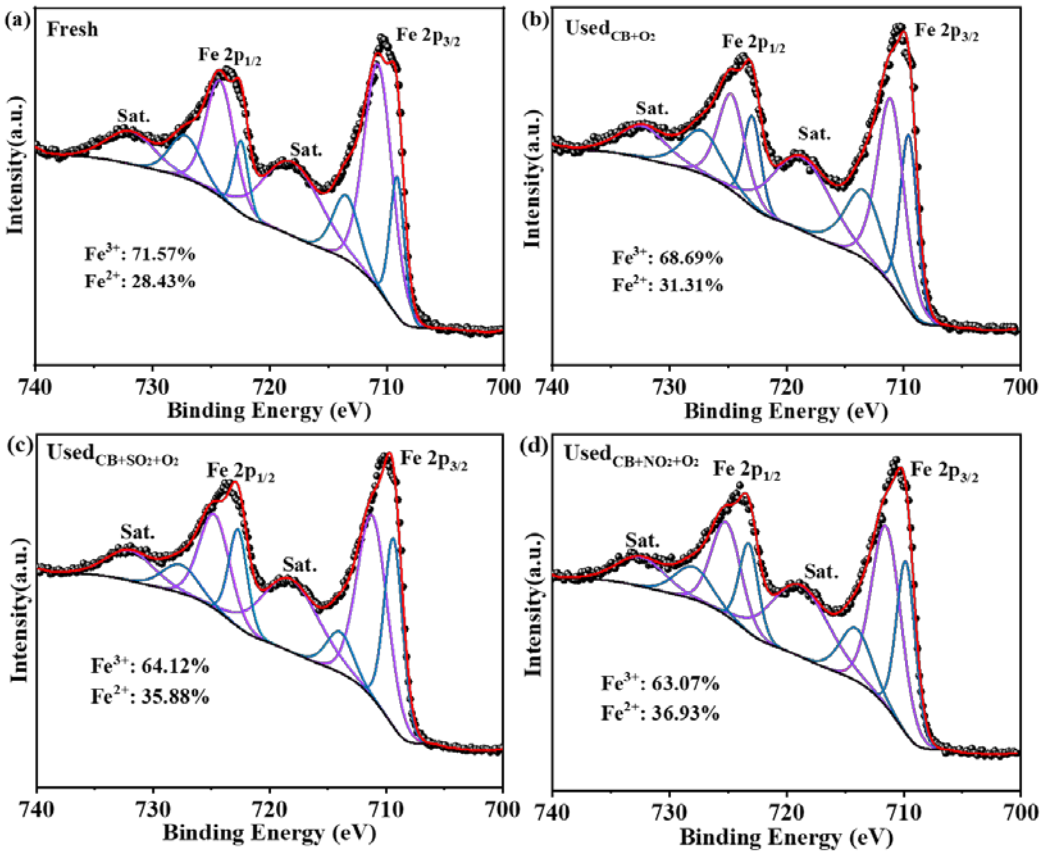

Figure S9. Fe 2p profiles of the reacted α-Fe_2O_3. (a) Fresh sample; (b) CB + O_2; (c) CB + SO_2 + O_2; (d) CB + NO_2 + O_2.

Following the previous study, curve fitting for Fe(II) and Fe(III) was conducted by first fixing the binding energy (BE) gap between $Fe2p_{1/2}$ and $Fe2p_{3/2}$ at approximately 13.45 eV and the intensity ratio at 0.5 (Pauly et al., 2019), which yielded the peak BE of Fe(III) at about 710.30-710.8 eV, approximately 1.25 eV higher than that of Fe(II), consistent with those reported by Sun *et al.* and Liao *et al.* (Sun et al., 2013; Liao et al., 2017). These two components, however, do not share the same full-width-at-half-maximum (FWHM), where the Fe(III) has a higher binding energy with the FWHM value at 2.5 ± 0.4 eV, while the Fe(II) is at a lower binding energy with the FWHM value at 1.2 ± 0.2 eV. Besides, the FWHM value of satellite peaks were usually at 3.5-6.0 eV (Zhang et al., 2013). Our normalize chi sqr (χ^2) was calculated at the range of 0.5-1.3, indicating the curve fitting was robust.

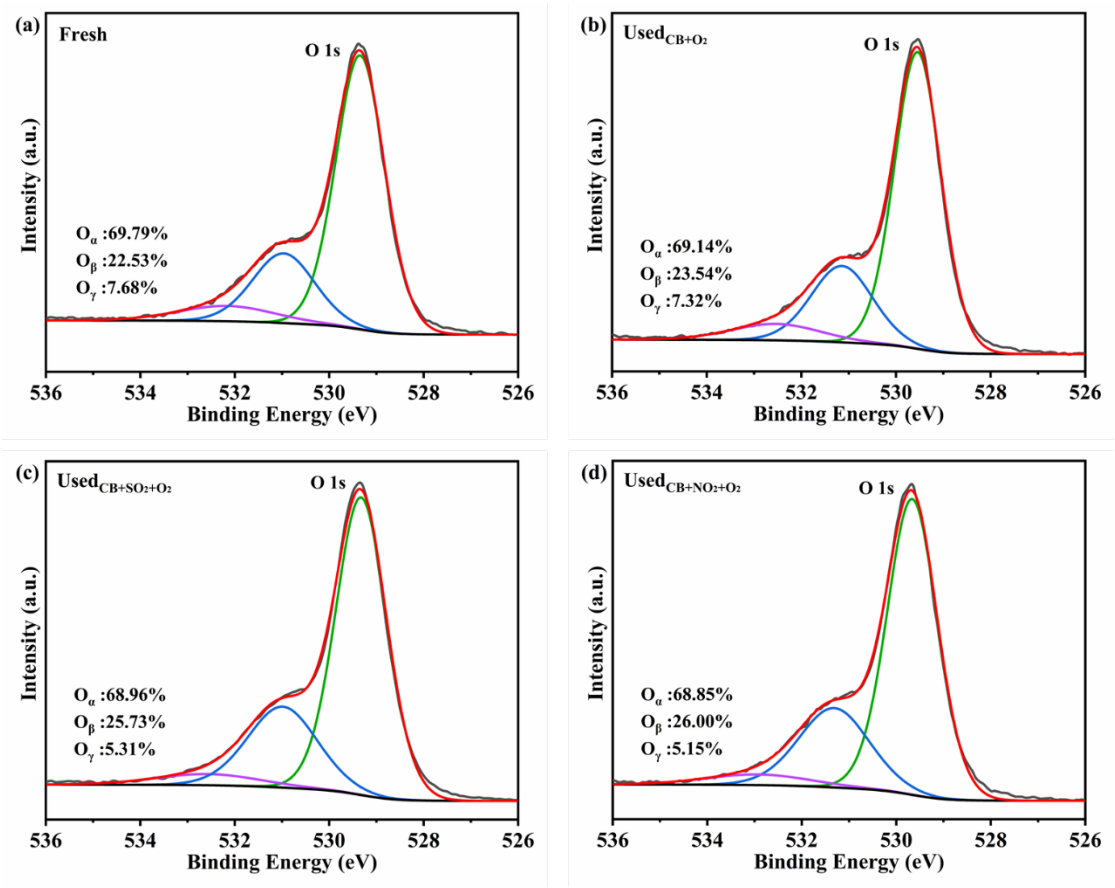

Figure S10. O 1s profiles of the reacted α-Fe_2O_3. (a) Fresh sample; (b) CB + O_2; (c) CB + SO_2 + O_2; (d) CB + NO_2 + O_2.

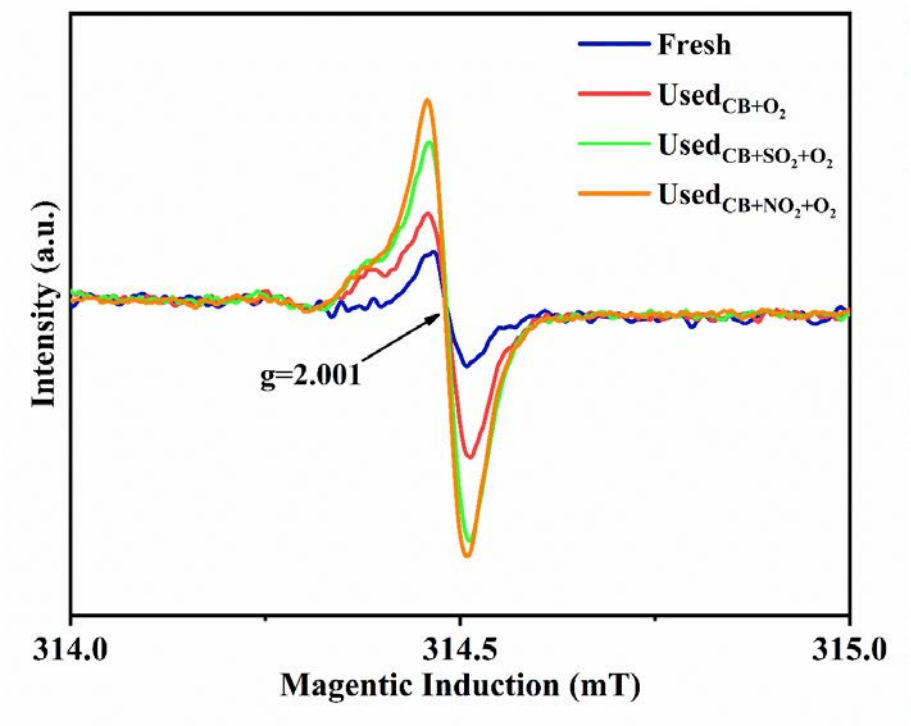

Figure S11. EPR spectra of the fresh and used α-Fe_2O_3.

Table S1. The list of gas phase intermediates tested.

Label	Species (Formula)	Molecular structure
1	Isopropanol (C_3H_8O)	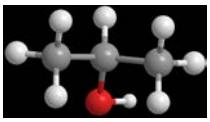
2	Methyl tert-butyl ether ($C_5H_{12}O$)	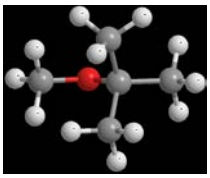
3	N-Hexane (C_6H_{14})	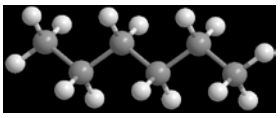
4	Carbon Tetrachloride (CCl_4)	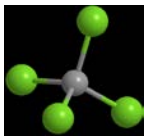
5	1,2-Dichloroethane ($C_2H_4Cl_2$)	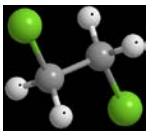
6	Benzene (C_6H_6)	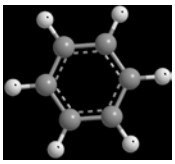
7	N-Heptane (C_7H_{16})	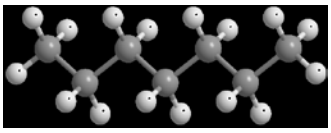
8	Trichloroethylene (C_2HCl_3)	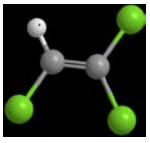
9	1,2-Dichloropropane ($C_3H_6Cl_2$)	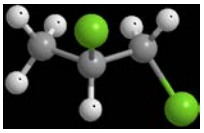

Label	Species (Formula)	Molecular structure
10	Methyl Methacrylate ($C_5H_8O_2$)	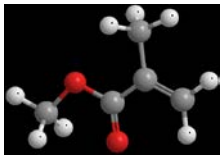
11	1,4-Dioxane ($C_4H_8O_2$)	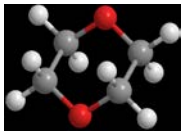
12	4-Methyl-2-Pentanone ($C_6H_{12}O$)	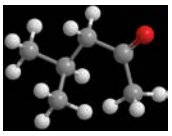
13	Toluene (C_7H_8)	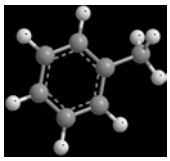
14	1,1,2-Trichloroethane ($C_2H_3Cl_3$)	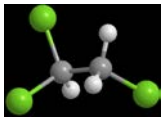
15	Perchloroethylene (C_2Cl_4)	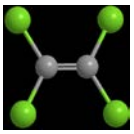
16	O-Xylene (C_8H_{10})	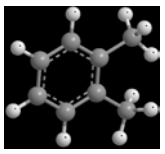
17	p-Dichlorobenzene ($C_6H_4Cl_2$)	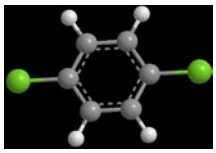

Table S2. The decay rate of CB on α-Fe_2O_3 under different relative humidity. Reaction conditions: [CB] =200 ppm, [O_2] = 20 vol%, 30 °C and xenon light irradiation (λ = 320–780 nm). (Note: The experiment in the last column was conducted under the actual atmospheric humidity.)

	CB+O_2+0%RH	**CB+O_2+70%RH**	**CB+O_2+100%RH**	**CB+O_2(ambient)**
k_0 (h^{-1})	0.0595±0.002	0.0602±0.004	0.02462±0.001	0.01421±0.002
k (h^{-1})	0.0769±0.004	0.08441±0.000	0.03207±0.001	0.03543±0.000
k-k_0 (h^{-1})	0.0174±0.004	0.02421±0.004	0.00745±0.001	0.02122±0.002

Table S3. The decay rate of CB on α-Fe_2O_3 under different initial CB concentrations. Reaction conditions: [O_2] = 20 vol%, 30 °C and xenon light irradiation (λ = 320–780 nm).

Initial concentration of CB	k_0 **(h^{-1})**	k **(h^{-1})**	k-k_0 **(h^{-1})**
200 ppm	0.01421±0.002	0.03543±0.000	0.02122±0.002
100 ppm	0.04314±0.002	0.06590±0.003	0.02276±0.004
50 ppm	0.07554±0.004	0.10243±0.001	0.02689±0.004

Table S4. The contents of PCDD/Fs accumulated on the reacted α-Fe_2O_3 surfaces under different reaction atmospheres. Reaction conditions: [CB] = 200 ppm, [SO_2] = [NO_2] = 50 ppm, air balance, 30 °C, 35 h and xenon light irradiation (λ = 320–780 nm).

	CB + O_2	**CB + SO_2 + O_2**	**CB + NO_2 + O_2**
∑PCDDs (ng I-TEQ kg^{-1})	9.506	0.717	0.304
∑PCDFs (ng I-TEQ kg^{-1})	14.445	1.309	0.105

Table S5. *In situ* DRIFT band assignments of the surface species.

Wavenumber (cm^{-1})						Assignments	Cite
CB+O_2-Dark	**CB+O_2-Light**	**CB+SO_2+O_2-Dark**	**CB+SO_2+O_2-Light**	**CB+NO_2+O_2-Dark**	**CB+NO_2+O_2-Light**		
3702	3702	3702	3702	3702	3705		
3667	3667	3670	3670	3668	3670	free OH	(Nagao and Suda, 1989)
3600	3600	3588	3588	3592	3589		
/	/	/	/	/	3064	C-H of aromatic ring	(Niu et al., 2017)
/	/	/	/	2083	/	CO of carboxylate	(Wang et al., 2019)
/	/	/	1877	1878	1872	aldehydes	(Wang et al., 2015)
1639	1650						
1394	1394	1394	1390	1394	1395	surface alkenes	(Deng et al., 2016)
1304	1304						
/	/	1676	1684	/	/	alkenes and the sulfate	(Deng et al., 2016; Zhang et al., 2020)
/	/	/	/	1658	1649	alkenes	(Deng et al., 2016)
/	/	/	1615	/	/	sulfate	(Zhang et al., 2020)
/	/	/	1584	/	/	C=C	(Lichtenberger and Amiridis, 2004)
1539	1539	/	1539	/	/	maleate	(Deng et al., 2016)

Wavenumber (cm^{-1})						Assignments	Cite
CB+O_2-Dark	**CB+O_2-Light**	**CB+SO_2+O_2-Dark**	**CB+SO_2+O_2-Light**	**CB+NO_2+O_2-Dark**	**CB+NO_2+O_2-Light**		
/	/	/	/	1539	1539	maleates or monodentate nitrates	(Deng et al., 2016; Niu et al., 2017; Du et al., 2019)
/	/	/	/	1521	1521	C-N asymmetric stretching vibration	(Niu et al., 2017)
1506	1506	/	1506	/	1506	benzene	(Sun et al., 2018)
/	/	1477	1479	/	/	C=C of phenolate and the gaseous SO_2	(Gu et al., 2019; Guan et al., 2021)
1477 1445	1477 1445	1445	1445	/	/	C=C of phenolate	(Gu et al., 2019)
/	/	/	/	1477	1477	C=C of phenolate and bridging monodentate nitrito NO_2^-	(Hixson et al., 2011; Kong et al., 2014; Gu et al., 2019)
/	/	/	/	1445	1445	C=C of phenolate and monodentate nitrito NO_2^-	(Hixson et al., 2011; Gu et al., 2019)
/	/	/	/	/	1417	benzene ring	(Lichtenberger and Amiridis, 2004)
1363 1334	1363 1334	1332	1332	/	/	—COOH	(Sun et al., 2018)
/	/	1363	1367	/	/	asymmetric S=O stretching vibration	(Wang et al., 2020)
/	/	/	/	1363	1362	water-soluble nitrates	(Niu et al., 2017; Du et al., 2019)

Wavenumber (cm^{-1})						Assignments	Cite
CB+O_2-Dark	**CB+O_2-Light**	**CB+SO_2+O_2-Dark**	**CB+SO_2+O_2-Light**	**CB+NO_2+O_2-Dark**	**CB+NO_2+O_2-Light**		
				1334	1336		
/	/	/	/	1302	1302	N_2O_4	(Niu et al., 2017; Du et al., 2019)
/	/	1298	1298	/	/	chelated bidentate inorganic SO_4^{2-}	(Liu et al., 2011)
/	1225	/	/	/	/	C—O of phenolate	(Deng et al., 2016; Sun et al., 2018)
/	/	1207	1211	/	/	monodentate sulfate	(Du et al., 2019)
/	/	/	/	1209	1207	nitrite	(Niu et al., 2017)
/	/	1154 1113	1156 1113	/	/	bidentate sulfate	(Du et al., 2019)

Table S6. *In situ* DRIFT band assignments of the surface species.

Wavenumber (cm^{-1})					Assignments	Cite
CB-Dark	**SO_2-Dark**	**SO_2+O_2-Dark**	**NO_2-Dark**	**NO_2+O_2-Dark**		
3702	3706	3702	3702	3702		
3667	3664	3667	3667	3669	free OH	(Nagao and Suda, 1989)
3595	3573	3573	3593	3565		
/	1662, 1606, 1250	1641	/	/	sulfate	(Zhang et al., 2020; He et al., 2021)
/	/	/	/	1623	NO_2 or bridging nitrates	(Niu et al., 2017)
1583	/	/	/	/	formate	(Wu et al., 2013)
/	/	/	1584	/	bidentate NO_3^-	(Kong et al., 2014; Yang et al., 2018)
1477, 1445	/	/	/	/	C=C of phenolate	(Gu et al., 2019)
/	1471	/	/	/	symmetrical stretching vibration of gaseous SO_2	(Guan et al., 2021)
/	/	/	1479	/	bridging monodentate nitrito NO_2^-	(Hixson et al., 2011; Kong et al., 2014)

Wavenumber (cm^{-1})					Assignments	Cite
CB-Dark	**SO_2-Dark**	**SO_2+O_2-Dark**	**NO_2-Dark**	**NO_2+O_2-Dark**		
/	/	/	1446	/	monodentate nitrito NO_2^-	(Hixson et al., 2011)
/	1391	/	/	/	chelating bidentate sulfate	(Yu et al., 2021)
/	1364, 1330	1363, 1330	/	/	asymmetric S=O stretching vibration	(Wang et al., 2020)
1334	/	/	/	/	—COOH	(Sun et al., 2018)
/	/	/	1334	1361, 1334	water-soluble nitrates	(Niu et al., 2017; Du et al., 2019)
/	1293	1306	/	/	chelated bidentate inorganic SO_4^{2-}	(Liu et al., 2011)
/	/	1201	/	/	monodentate sulfate	(Du et al., 2019)
/	1157	/	/	/	bidentate sulfate	(Du et al., 2019)
/	/	/	/	1304	N_2O_4	(Niu et al., 2017; Du et al., 2019)
/	/	/	/	1203	nitrite	(Niu et al., 2017)

References

Blochl P E (1994). Projector augmented-wave method. Physical Review B, 50(24): 17953-17979

Deng W, Dai Q G, Lao Y J, Shi B B, Wang X Y (2016). Low temperature catalytic combustion of 1,2-dichlorobenzene over CeO_2-TiO_2 mixed oxide catalysts. Applied Catalysis B-Environmental, 181: 848-861

Du C T, Kong L D, Zhanzakova A, Tong S Y, Yang X, Wang L, Fu H B, Cheng T T, Chen J M, Zhang S C (2019). Impact of adsorbed nitrate on the heterogeneous conversion of SO_2 on α-Fe_2O_3 in the absence and presence of simulated solar irradiation. Science of the Total Environment, 649(1): 1393-1402

Feng Y C, Wang N N, Guo X, Zhang S X (2020a). Characteristics of dopant distribution and surface oxygen vacancy formation for modified Fe_2O_3 in chemical looping combustion. Fuel, 276: 117942

Feng Y C, Wang N N, Guo X, Zhang S X (2020b). Dopant screening of modified Fe_2O_3 oxygen carriers in chemical looping hydrogen production. Fuel, 262: 116489

Gu Y F, Cai T, Gao X H, Xia H Q, Sun W, Zhao J, Dai Q G, Wang X Y (2019). Catalytic combustion of chlorinated aromatics over WO_x/CeO_2 catalysts at low temperature. Applied Catalysis B-Environmental, 248: 264-276

Guan J K, Zhou L S, Li W Q, Hu D, Wen J, Huang B C (2021). Improving the performance of Gd addition on catalytic activity and SO_2 resistance over MnOx/ZSM-5 catalysts for low-temperature NH_3-SCR. Catalysts, 11(3): 324

Han L H, Chen Y Y, Jia L, Cheng S Y, Xu Y F, Ning H B, Zhang P (2014). Heterogeneous reactions of NO_2 on the surface of MgO particles. Scientia Sinica Chimica, 44(12): 2004-2012

He X, Wu J J, Ma Z C, Xi X, Zhang Y H (2021). NH_3-promoted heterogeneous reaction of SO_2 to sulfate on alpha-Fe_2O_3 particles with coexistence of NO_2 under different relative humidities. Atmospheric Environment, 262(1): 118622

Hixson B C, Jordan J W, Wagner E L, Bevsek H M (2011). Reaction products and kinetics of the reaction of NO_2

with gamma-Fe_2O_3. Journal of Physical Chemistry A, 115(46): 13364-13369

Kong L D, Zhao X, Sun Z Y, Yang Y W, Fu H B, Zhang S C, Cheng T T, Yang X, Wang L, Chen J M (2014). The effects of nitrate on the heterogeneous uptake of sulfur dioxide on hematite. Atmospheric Chemistry and Physics, 14(17): 9451-9467

Kresse G, Furthmuller J (1996). Efficiency of ab-initio total energy calculations for metals and semiconductors using a plane-wave basis set. Computational Materials Science, 6(1): 15-50

Kresse G, Hafner J (1993). Abinitio molecular-dynamics for liquid-metals. Physical Review B, 47(1): 558-561

Kresse G, Hafner J (1994). Ab-initio molecular-dynamics simulation of the liquid-metal amorphous-semiconductor transition in germanium. Physical Review B, 49(20): 14251-14269

Liao A Z, He H C, Fan Z W, Xu G Z, Li L, Chen J N, Han Q T, Chen X Y, Zhou Y, Zou Z G (2017). Facile room-temperature surface modification of unprecedented FeB co-catalysts on Fe_2O_3 nanorod photoanodes for high photoelectrochemical performance. Journal of Catalysis, 352: 113-119

Lichtenberger J, Amiridis M D (2004). Catalytic oxidation of chlorinated benzenes over V_2O_5/TiO_2 catalysts. Journal of Catalysis, 223(2): 296-308

Liu F D, Asakura K, He H, Shan W P, Shi X Y, Zhang C B (2011). Influence of sulfation on iron titanate catalyst for the selective catalytic reduction of NO_x with NH_3. Applied Catalysis B-Environmental, 103(3-4): 369-377

Nagao M, Suda Y (1989). Adsorption of benzene, toluene, and chlorobenzene on titanium-dioxide. Langmuir, 5(1): 42-47

Niu H J Y, Li K Z, Chu B W, Su W K, Li J H (2017). Heterogeneous reactions between toluene and NO_2 on mineral particles under simulated atmospheric conditions. Environmental Science & Technology, 51(17): 9596-9604

Pauly N, Yubero F, Espinós J P, Tougaard S (2019). XPS primary excitation spectra of Zn 2p, Fe 2p, and Ce 3d from ZnO, α-Fe_2O_3, and CeO_2. Surface and Interface Analysis, 51(3): 353-360

Perdew J P, Burke K, Ernzerhof M (1996). Generalized gradient approximation made simple. Physical Review Letters, 77(18): 3865-3868

Sun P F, Wang W L, Weng X L, Dai X X, Wu Z B (2018). Alkali potassium induced HCl/CO_2 selectivity enhancement and chlorination reaction inhibition for catalytic oxidation of chloroaromatics. Environmental Science & Technology, 52(11): 6438-6447

Sun W T, Meng Q Q, Jing L Q, Liu D N, Cao Y (2013). Facile synthesis of surface-modified nanosized α-Fe_2O_3 as efficient visible photocatalysts and mechanism insight. Journal of Physical Chemistry C, 117(3): 1358-1365

Wang J, Wang X, Liu X L, Zeng J L, Guo Y Y, Zhu T Y (2015). Kinetics and mechanism study on catalytic oxidation of chlorobenzene over V_2O_5/TiO_2 catalysts. Journal of Molecular Catalysis A-Chemical, 402: 1-9

Wang X W, Jiang W Y, Yin R Q, Sun P F, Lu Y H, Wu Z B, Weng X L (2020). The role of surface sulfation in mediating the acidity and oxidation ability of nickel modified ceria catalyst for the catalytic elimination of chlorinated organics. Journal of Colloid and Interface Science, 574: 251-259

Wang Z W, Li S, Xie S H, Liu Y X, Dai H X, Guo G S, Deng J G (2019). Supported ultralow loading Pt catalysts with high H_2O-, CO_2-, and SO_2-resistance for acetone removal. Applied Catalysis A-General, 579(5): 106-115

Wu L Y, Tong S R, Zhou L, Wang W G, Ge M F (2013). Synergistic effects between SO_2 and HCOOH on alpha-Fe_2O_3. Journal of Physical Chemistry A, 117(19): 3972-3979

Yang W W, Ma Q X, Liu Y C, Ma J Z, Chu B W, Wang L, He H (2018). Role of NH_3 in the heterogeneous formation of secondary inorganic aerosols on mineral oxides. Journal of Physical Chemistry A, 122(30): 6311-6320

Yu Y X, Tan W, An D Q, Wang X W, Liu A N, Zou W X, Tang C J, Ge C Y, Tong Q, Sun J F, Dong L (2021). Insight into the SO_2 resistance mechanism on gamma-Fe_2O_3 catalyst in NH_3-SCR reaction: A collaborated experimental and DFT study. Applied Catalysis B-Environmental, 281: 119544

Zhang Y P, Li G B, Wu P, Zhuang K, Huang T J (2020). Effect of SO_2 on the low-temperature denitrification

performance of Ho-modified Mn/Ti catalyst. Chemical Engineering Journal, 400(15): 122597

Zhang Z, Lu J P, Yun T, Zheng M R, Pan J S, Sow C H, Tok E S (2013). Desorption of ambient gas molecules and phase transformation of α-Fe_2O_3 nanostructures during ultrahigh vacuum annealing. Journal of Physical Chemistry C, 117(3): 1509-1517